Heterogeneous Enhancement Patterns of Tumor-adjacent Parenchyma at MR Imaging Are Associated with Dysregulated Signaling Pathways and Poor Survival in Breast Cancer[1]

Jia Wu, PhD
Bailiang Li, PhD
Xiaoli Sun, MD
Guohong Cao, MD
Daniel L. Rubin, MD, MS
Sandy Napel, PhD
Debra M. Ikeda, MD
Allison W. Kurian, MD, MSc
Ruijiang Li, PhD

Purpose: To identify the molecular basis of quantitative imaging characteristics of tumor-adjacent parenchyma at dynamic contrast material–enhanced magnetic resonance (MR) imaging and to evaluate their prognostic value in breast cancer.

Materials and Methods: In this institutional review board-approved, HIPAA-compliant study, 10 quantitative imaging features depicting tumor-adjacent parenchymal enhancement patterns were extracted and screened for prognostic features in a discovery cohort of 60 patients. By using data from The Cancer Genome Atlas (TCGA), a radiogenomic map for the tumor-adjacent parenchymal tissue was created and molecular pathways associated with prognostic parenchymal imaging features were identified. Furthermore, a multigene signature of the parenchymal imaging feature was built in a training cohort (n = 126), and its prognostic relevance was evaluated in two independent cohorts (n = 879 and 159).

Results: One image feature measuring heterogeneity (ie, information measure of correlation) was significantly associated with prognosis (false-discovery rate < 0.1), and at a cutoff of 0.57 stratified patients into two groups with different recurrence-free survival rates (log-rank P = .024). The tumor necrosis factor signaling pathway was identified as the top enriched pathway (hypergeometric P < .0001) among genes associated with the image feature. A 73-gene signature based on the tumor profiles in TCGA achieved good association with the tumor-adjacent parenchymal image feature (R^2 = 0.873), which stratified patients into groups regarding recurrence-free survival (log-rank P = .029) and overall survival (log-rank P = .042) in an independent TCGA cohort. The prognostic value was confirmed in another independent cohort (Gene Expression Omnibus GSE 1456), with log-rank P = .00058 for recurrence-free survival and log-rank P = .0026 for overall survival.

Conclusion: Heterogeneous enhancement patterns of tumor-adjacent parenchyma at MR imaging are associated with the tumor necrosis signaling pathway and poor survival in breast cancer.

Online supplemental material is available for this article.

[1] From the Department of Radiation Oncology (J.W., B.L., R.L.), Department of Radiology (D.L.R., S.N., D.M.I.), Department of Biomedical Data Science and Medicine (Biomedical Informatics Research) (D.L.R.), Department of Medicine (A.W.K.), Department of Health Research and Policy (A.W.K.), and Stanford Cancer Institute (A.W.K., R.L.), Stanford University School of Medicine, 1070 Arastradero Rd, Stanford, CA 94305; Department of Radiotherapy, the First Affiliated Hospital of Zhejiang University, Hangzhou, Zhejiang, China (X.S.); and Department of Radiology, International Hospital of Zhejiang University, Hangzhou, Zhejiang, China (G.C.). Received December 14, 2016; revision requested February 4, 2017; revision received February 16; accepted March 29; final version accepted May 4. **Address correspondence to** R.L. (e-mail: *rli2@stanford.edu*).

This research was partially supported by the National Cancer Institute (R01 CA193730) and the National Institutes of Health Clinical Center (U01 CA187947).

Breast cancer is the most common noncutaneous malignancy in women. Around 20%–30% of women diagnosed with invasive breast cancer will have a metastatic recurrence and may eventually die of this disease (1). Adjuvant chemotherapy reduces the absolute rate of recurrence by up to 5 percentage points and is recommended for a majority of patients with invasive breast cancer (2,3). However, not all patients derive benefit from chemotherapy, given its toxicity and side effects (4). Reliable prognostic biomarkers are needed to identify patients who are at low risk of recurrence and to reduce overtreatment with chemotherapy.

Dynamic contrast material–enhanced magnetic resonance (MR) imaging is clinically used for the diagnosis and evaluation of treatment response in breast cancer. Quantitative image features such as tumor size, shape, margin, and kinetics have been shown to improve on or augment the opinions of human experts for diagnostic purposes (5–9). Recently, tumor texture features have also been investigated (10–14). However, their prognostic accuracy appears to be limited for predicting disease recurrence and survival (15,16). An important limitation of existing studies is that the image analysis was focused on the tumor, while the surrounding tissues were ignored.

Several recent studies have demonstrated that global enhancement patterns of background parenchyma at dynamic contrast-enhanced MR imaging are associated with the risk of developing breast cancer in a screening population (17–21), and with response to chemotherapy (22), disease-free survival, and overall survival (23) in patients with invasive breast cancer. Furthermore, because breast cancer invades its neighboring tissue and induces extensive remodeling during tumor progression (24), enhancement patterns of tumor-adjacent parenchyma at dynamic contrast-enhanced MR imaging have also been associated with response to chemotherapy (25) and local recurrence (26). Yet the biologic underpinning of parenchymal imaging characteristics is poorly understood, and their clinical relevance requires further validation.

The purpose of this study was to identify the molecular basis of quantitative imaging characteristics of tumor-adjacent parenchyma at dynamic contrast-enhanced MR imaging and to evaluate their prognostic value in breast cancer.

Advances in Knowledge

- A 73-gene signature of the tumor-adjacent parenchymal image feature stratified patients into low-risk versus high-risk groups in terms of recurrence-free survival (log-rank $P = .029$, hazard ratio [HR] = 1.54, 95% confidence interval [CI]: 1.03, 2.29) and overall survival (log-rank $P = .042$, HR = 1.51, 95% CI: 1.02, 2.28) in an independent The Cancer Genome Atlas testing cohort ($n = 879$).
- The multigene signature stratified an independent gene expression cohort (Gene Expression Omnibus GSE 1456, $n = 159$) into low-risk versus high-risk groups in terms of recurrence-free survival (log-rank $P = .00058$, HR = 2.84, 95% CI: 1.53, 5.29) and overall survival (log-rank $P = .0026$, HR = 2.92, 95% CI: 1.40, 6.08).

Materials and Methods

Study Design

In this institutional review board–approved, Health Insurance Portability and Accountability Act–compliant study, we investigated the prognostic performance of quantitative imaging phenotypes that characterize the enhancement patterns of tumor-adjacent parenchyma and explored the underlying molecular basis of the prognostic imaging feature. We performed this study in three steps (Fig 1a).

Implication for Patient Care

- Breast cancer with greater parenchymal enhancement heterogeneity at dynamic contrast-enhanced MR imaging may be associated with inflammatory response and tends to have a poor prognosis.

First, we extracted quantitative imaging features depicting tumor-adjacent parenchymal enhancement patterns and screened for those that were potentially prognostic for survival. Second, we created a radiogenomic map to link prognostic imaging features of the tumor-adjacent parenchyma with associated molecular pathways. Finally, we built a multigene signature of the parenchymal imaging feature and aimed to validate its prognostic value by leveraging large, publicly available genomic data sets.

Patient Population

The prognostic imaging biomarker discovery was based on a retrospective single-institution cohort of 60 patients with invasive breast cancer, for whom the pretreatment dynamic contrast-enhanced MR imaging and recurrence-free survival (RFS) data are publicly available at The Cancer Imaging Archive (TCIA) (27). The details of this cohort have been published (28,29). A multi-institution cohort from The Cancer Genome Atlas (TCGA) (30) was used in the radiogenomic discovery and validation steps. The patient data are

https://doi.org/10.1148/radiol.2017162823

Content codes: BR MR OI

Radiology 2017; 285:401–413

Abbreviations:
CI = confidence interval
FDR = false-discovery rate
FTV = functional tumor volume
HR = hazard ratio
KEGG = Kyoto Encyclopedia of Genes and Genomes
RFS = recurrence-free survival
SER = signal enhancement ratio
TCGA = The Cancer Genome Atlas
TNF = tumor necrosis factor
WGCNA = weighted gene coexpression network analysis

Author contributions:
Guarantors of integrity of entire study, J.W., X.S., G.C., R.L.; study concepts/study design or data acquisition or data analysis/interpretation, all authors; manuscript drafting or manuscript revision for important intellectual content, all authors; manuscript final version approval, all authors; agrees to ensure any questions related to the work are appropriately resolved, all authors; literature research, J.W., B.L., G.C., D.M.I., R.L.; clinical studies, J.W., X.S., G.C., D.M.I.; experimental studies, J.W., X.S., G.C., R.L.; statistical analysis, J.W., B.L., G.C.; and manuscript editing, J.W., B.L., G.C., D.L.R., S.N., D.M.I., A.W.K., R.L.

Conflicts of interest are listed at the end of this article.

Figure 1

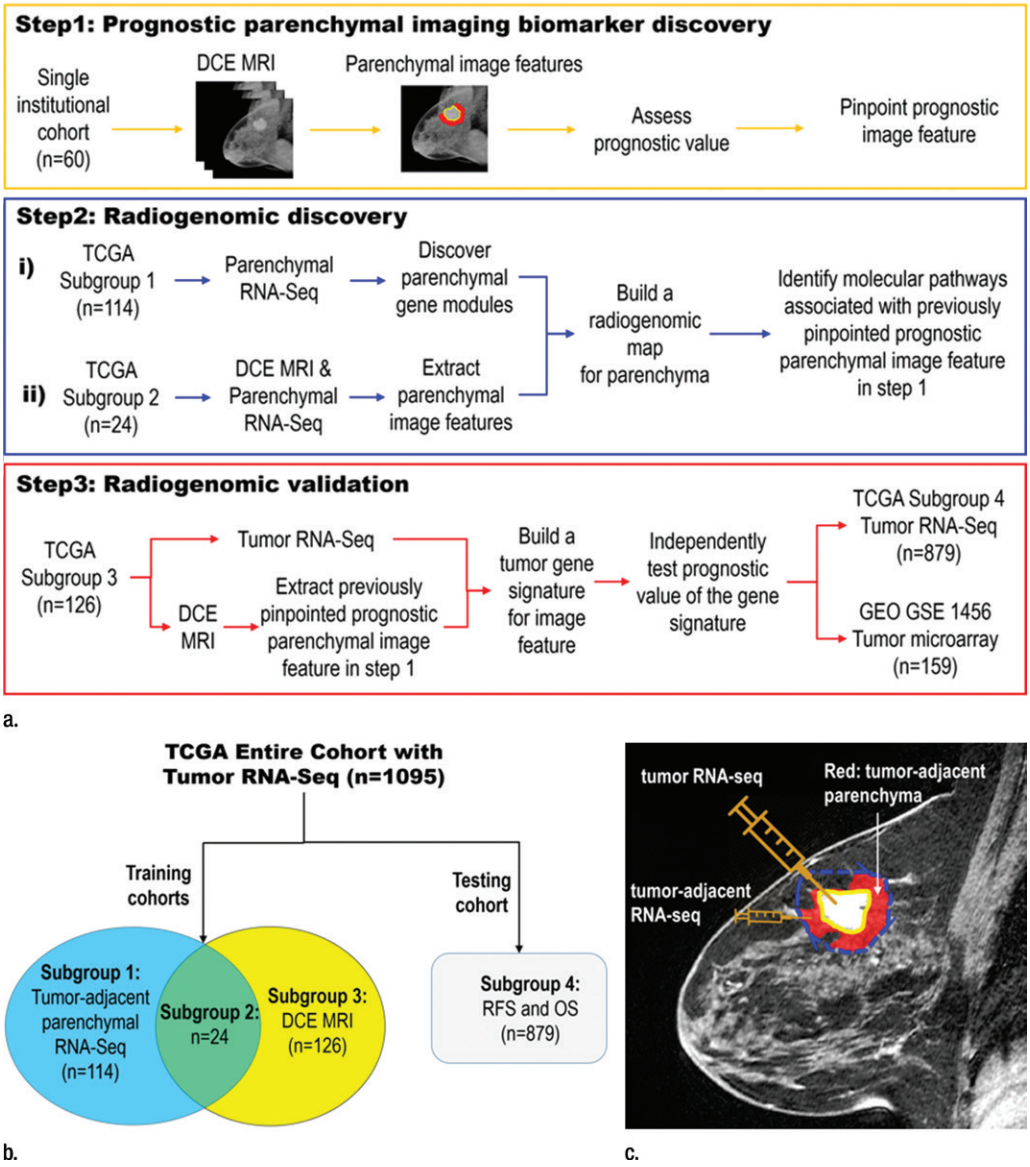

Figure 1: **(a)** Flowchart of the overall design for the radiogenomic study, which involves three key steps. **(b)** Venn diagram of the TCGA data composition and four subgroups. **(c)** The acquisition protocol for tumor and parenchymal RNA sequencing *(RNA-Seq)* data in TCGA. The tumor-adjacent parenchyma is defined as the red region, where the yellow line is the tumor boundary and the blue dotted line is the dilated tumor boundary of 2 cm. *DCE* = dynamic contrast enhanced, *GEO* = Gene Expression Omnibus, *OS* = overall survival.

summarized in Figure 1b. A total of 1095 patients with invasive breast cancer were included, all of whom had RNA sequencing data available for tumor samples. RNA sequencing data for tumor-adjacent, pathologically normal parenchyma (<2 cm) (31) were available for 114 patients (subgroup 1), and pretreatment dynamic contrast-enhanced MR imaging data were available for 126 patients (subgroup 3) through the Genomic Data Commons data portal and TCIA (27,32). Twenty-four patients in TCGA (subgroup 2) had both tumor-adjacent gene expression and dynamic contrast-enhanced MR imaging data available. In addition to data in these three subgroups, data in a separate group of 879 patients (subgroup 4) with clinical outcome data were used for independent testing purposes. The genomic data acquisition method is shown in Figure 1c. In addition, another independent breast cancer cohort (GSE 1456, $n = 159$) with publicly available microarray gene

expression data and clinical outcomes (overall survival and RFS) were used in the final validation stage through the Gene Expression Omnibus. Details of this cohort have been published (33). The demographic and clinical information for all three cohorts is summarized in Table 1, and information for the three TCGA subgroups is presented in Table E1 (online).

Segmentation of Tumor-adjacent Parenchyma

Tumor-adjacent parenchyma was defined as parenchyma that falls within a 2-cm distance to the tumor boundary. This definition is spatially congruent with the acquisition of RNA sequencing data for the tumor-adjacent tissue in TCGA (31). Similarly, another imaging and histologic correlative study also used a 2-cm distance to the tumor margin for defining cancer-associated stroma in breast cancer (34). For tumor segmentation, two radiologists (G.C. and X.S., with 17 and 11 years of experience in breast imaging, respectively) manually delineated the tumor section-by-section in consensus. Next, we used fuzzy c-means clustering (32) to automatically segment the entire breast region into fatty tissue and nonfatty tissue. The ipsilateral breast parenchyma was defined as the nonfatty tissue region excluding the tumor and was confirmed by both radiologists in consensus. Finally, we dilated the tumor contours by 2 cm in three dimensions using a $3 \times 3 \times 3$ 6-connected kernel (35), and the intersection between this hollow sphere structure and the breast parenchyma was defined as the tumor-adjacent parenchyma.

Extraction of Tumor-adjacent Parenchymal Image Features

Ten quantitative image features were extracted to characterize the degree and heterogeneity of contrast-enhancing patterns of the tumor-adjacent parenchyma. We first extracted the signal enhancement ratio (SER) maps from three sequential dynamic contrast-enhanced MR images—precontrast, early postcontrast (around 2.5 minutes), and late postcontrast (around 7.5 minutes). Then we calculated three relative enhancing volumes (16), two histogram-based features (23,25,26), and five Haralick features

Table 1

Demographic and Clinical Data of the Study Cohorts

Parameter	Imaging Biomarker Discovery Cohort ($n = 60$)	TCGA Cohort ($n = 1095$)	GSE 1456 Cohort ($n = 159$)
Age (y)			
Median*	48.1 (29.7–72.4)	58 (26–90)	…
Mean ± standard deviation	48.0 ± 9.9	58.0 ± 13.2	58 ± 13.6
Race			
Asian	4 (7)	61 (6)	…
Black or African American	3 (5)	183 (17)	…
White	45 (75)	757 (69)	…
Unknown or others	8 (13)	1 (0)	…
Estrogen receptor status			
Positive	28 (47)	601 (55)	130 (82)
Negative	20 (33)	179 (16)	29 (18)
Indeterminate	0	2 (0)	0 (0)
Unknown	12 (20)	313 (29)	0 (0)
Progesterone receptor status			
Positive	22 (37)	522 (48)	114 (72)
Negative	26 (43)	255 (23)	45 (28)
Indeterminate	0	4 (0)	0 (0)
Unknown	12 (20)	314 (29)	0 (0)
Human epidermal growth factor receptor 2 status			
Positive	14 (23)	114 (10)	…
Negative	31 (52)	652 (60)	…
Equivocal	0	10 (1)	…
Unknown	15 (25)	319 (29)	…
Histologic type			
Infiltrating ductal carcinoma	37 (62)	780 (71)	…
Infiltrating lobular carcinoma	11 (18)	190 (17)	…
Other	12 (20)	104 (9)	…
Unknown	0	21 (2)	…
Surgery type			
Lumpectomy	27 (45)	266 (24)	…
Mastectomy	33 (55)	504 (46)	…
Other	0	252 (23)	…
Unknown	0	73 (7)	…
Follow-up (y)†			
Median*	6.67 (0.95–9.84)	2.17 (0.03–23.58)	7.47 (0.23–8.49)
Mean ± standard deviation	6.05 ± 2.35	3.33 ± 3.19	6.97 ± 1.46
Recurrence‡			
Event	22 (37)	113 (10)	40 (25)
No event	37 (62)	689 (63)	119 (75)
Unknown	1 (2)	293 (27)	0 (0)
Death†			
Event	…	149 (14)	29 (18)
No event	…	923 (84)	130 (82)
Unknown	….	23 (2)	0 (0)

Note.—Unless otherwise indicated, data are numbers of patients, with percentages in parentheses.

* Data in parentheses are the range.

† Computed with subjects alive.

‡ Follow-up data were updated in April 2017 through the Genomic Data Commons Data Portal.

Table 2

Details of 10 Quantitative Image Features Extracted from Tumor-adjacent Parenchyma from Dynamic Contrast-enhanced MR Imaging

Type, No., and Name	Interpretation
Volume ($n = 3$)	
1. $Prop_{SER>0.5}$, 2. $Prop_{SER>1.0}$, and 3. $Prop_{SER>1.5}$	Measure the relative enhanced volume of tumor-adjacent region on the basis of the selected threshold. Different SER threshold values correspond to the different kinetic type of contrast enhancement, with 0.5 as persistent, 1.0 as plateau, and 1.5 as washout.
Enhancing signal value ($n = 2$)	
1. $\overline{SER}_{1\%}$, 2. $\overline{SER}_{100\%}$	Mean value of the SER of tumor-adjacent parenchyma in top 1% and all (100%) voxels.
Texture (GLCM, $n = 5$)	
1. Dissimilarity, 2. Energy, 3. Entropy, 4. Homogeneity, and 5. Information measure of correlation	Measure the spatial heterogeneity of intensity value of the SER map within the tumor-adjacent region with five independent Haralick features.

Notes.—SER is defined as $SER = \frac{I_{\text{early postcontrast}} - I_{\text{precontrast}}}{I_{\text{late postcontrast}} - I_{\text{precontrast}}}$; GLCM = gray-level co-occurrence matrix. Relative volume is defined as $\frac{V_{>\text{cutoff}}}{V_{\text{all}}} \cdot 100\%$. A detailed formulation of each GLCM texture feature can be found at (37), and information measure of correlation refers to the second one.

(36) that measure the textural heterogeneity based on the gray-level co-occurrence matrix. The name of each image feature, as well as its formulation, is listed in Table 2. To minimize variations due to different acquisition protocols in different cohorts, we applied a series of image processing algorithms before feature extraction, including removal of shading artifacts (38), normalization of the MR imaging data (39), and resampling images to an isotropic spatial resolution of 0.8 mm (see details in Appendix E1 [online]). All image processing and feature extraction processes were performed in MATLAB (MathWorks, Natick, Mass).

Assessment of the Prognostic Value of Parenchymal Image Features and Independence from Tumor Features

In the imaging biomarker discovery cohort, each image feature was individually evaluated for its association with RFS. We then performed a two-step analysis to identify the image feature that had the strongest independent association with RFS. First, we identified the feature pairs that had a strong linear relationship based on Pearson correlation coefficients (>0.7). For correlated feature pairs, only the one with higher prognostic power in the univariate analysis was retained. Second, a multivariate Cox regression model was fitted with uncorrelated features to determine which image features were independently associated with RFS.

Three previously reported image features were extracted to characterize the tumor, including gross volume (40), functional tumor volume (FTV) (16), and SER (41–43). We first investigated the linear correlation (Pearson) between the three tumor features and uncorrelated parenchymal features. Then, a multivariate analysis was performed to determine whether parenchymal image features were independently associated with RFS in addition to tumor features. $P < .05$ was considered to indicate a statistically significant difference in multivariate analysis.

Identification of Gene Modules for Tumor-adjacent Parenchymal Tissue

To reduce gene data dimensionality and obtain more reliable results, we used an established technique called weighted gene coexpression network analysis (WGCNA) (44) to identify a small number of gene modules—that is, clusters of closely connected genes. Compared with conventional clustering approaches, WGCNA has been shown to be more robust because it considers both correlation and topologic information (44). First, the RNA sequencing data for 114 tumor-adjacent parenchymal tissue samples in TCGA were preprocessed to remove the genes with 80% or more missing or zero expression values. Then, the RNA sequencing data for the top 5000 genes with the largest variance were normalized to identify gene modules by using the WGCNA R package (detailed configuration in Appendix E1 [online]). Each module was summarized by its first principal component of the scaled (standardized) module expression profiles, as the module eigengene explains the maximum amount of variation of the module expression levels.

Construction of a Radiogenomic Map for Tumor-adjacent Parenchymal Tissue

Using TCGA data of the 24 samples that had tumor-adjacent parenchymal RNA sequencing and dynamic contrast-enhanced MR imaging data, we created a radiogenomic association map that links parenchymal imaging features with gene modules that were both extracted from tumor-adjacent tissue. The Pearson linear correlation was computed to assess the association between each imaging feature and each gene module. On the basis of this map, we pinpointed the tumor-adjacent parenchymal gene module associated with the image feature that showed prognostic significance in the imaging biomarker discovery cohort, adjusting for multiple hypothesis testing (45). The list of genes within the identified gene module was put into the Kyoto Encyclopedia of Genes and Genomes (KEGG) pathway analysis (46) to find the significantly enriched molecular pathways and to explore the biologic meaning of the parenchymal imaging feature.

Construction of a Tumor Gene Expression Signature for the Parenchymal Image Feature

On the basis of the assumption that the tumor is the driving force behind the

Figure 2

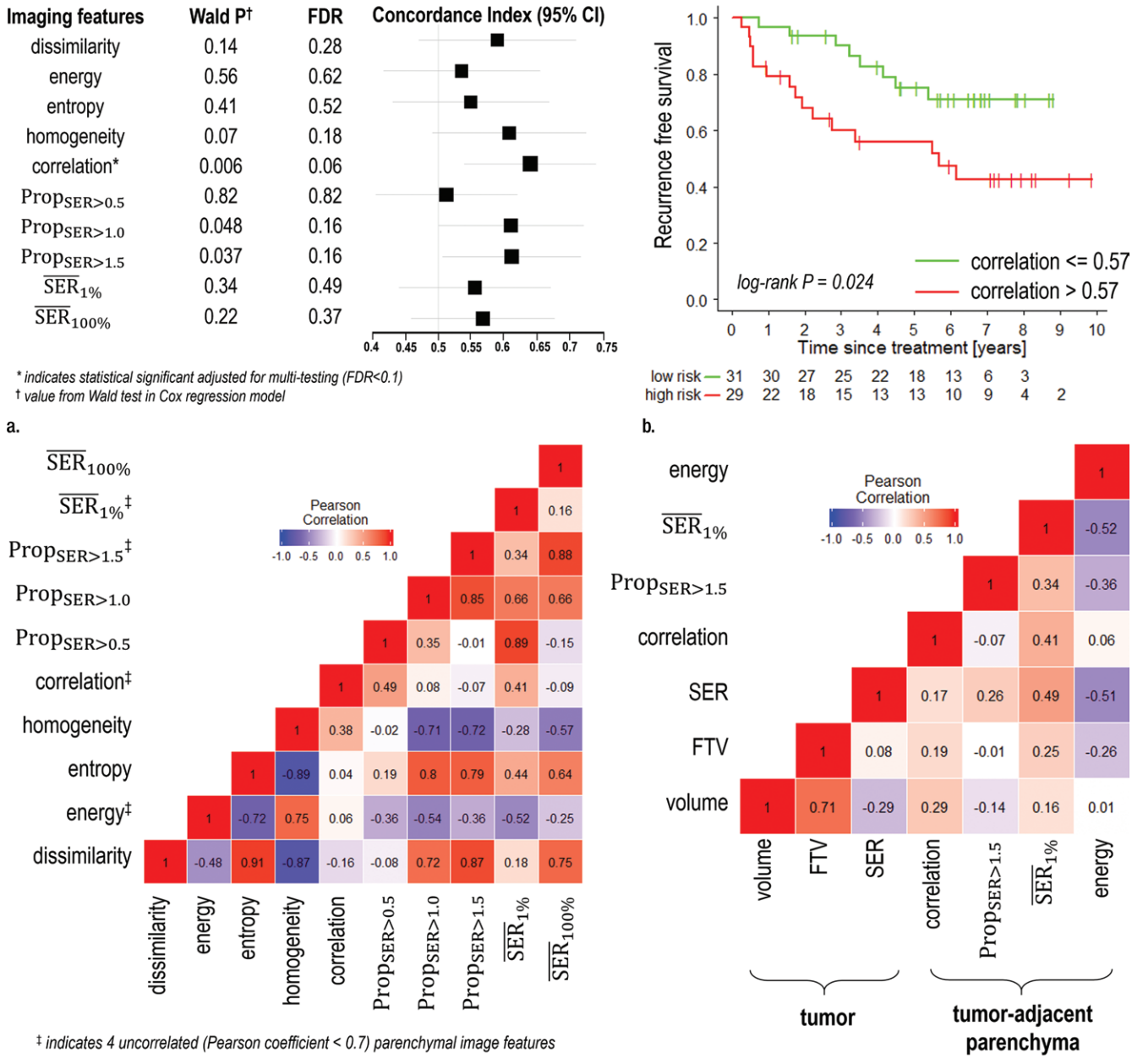

Figure 2: Images for the prognostic imaging biomarker discovery cohort ($n = 60$). **(a)** Graph shows prognostic performance for each of 10 quantitative tumor-adjacent parenchymal features from dynamic contrast-enhanced MR imaging. **(b)** Kaplan-Meier curves of RFS with the significantly prognostic (FDR < 0.1) quantitative imaging feature (information measure of correlation). **(c)** Pearson correlation matrix for 10 tumor-adjacent parenchymal imaging features, where four of them are uncorrelated. **(d)** Pearson correlation matrix for four uncorrelated tumor-adjacent parenchymal features and three tumor imaging features.

aberrant gene expression and abnormal imaging appearance in the surrounding tissue, we built a multigene signature to find associations with parenchymal imaging features by using gene expression data within the tumor. On the basis of findings in 126 patients with dynamic contrast-enhanced MR imaging and tumor gene expression data available in TCGA, we first identified the top 100 genes most correlated with the parenchymal image feature that showed

prognostic significance in the imaging biomarker discovery cohort. Then, a linear regression model nested with the backward feature selection was implemented to build the gene signature, where repeated 10-fold cross validation was applied to reduce potential selection bias and model overfitting (see details in Appendix E1 [online]). The tumor genes that constitute the signature were investigated with KEGG pathway enrichment analysis to confirm the previously identified pathways that are enriched in parenchymal tissue. Results were further compared with the enriched molecular pathways identified by using data for the TCGA testing cohort (subgroup 4).

Validation of the Prognostic Value of the Gene Signature for the Parenchymal Image Feature

Using the tumor gene expression–based signature for the parenchymal image feature, we tested its prognostic capability by assessing association with overall survival and RFS in two independent cohorts, including the separate TCGA testing cohort (subgroup 4) and another breast cancer cohort from the Gene Expression Omnibus (GSE 1456). Because some genes in the signature were missing for GSE 1456, we adopted a different validation strategy: On the basis of the measured genes in the signature, we applied hierarchic clustering to divide the whole population into subgroups, we labeled the subgroups as high risk or low risk on the basis of patterns of overlapped genes in TCGA cohort, and we then investigated whether these two subgroups had significantly different prognoses. For hierarchic clustering, the Ward method (47) and Euclidean distance were selected, and gap statistics (48) were used to determine the cluster number.

Statistical Analysis

The Cox proportional hazards model was used to build survival models associated with either overall survival or RFS. Kaplan-Meier analysis was used to estimate survival probability. On the basis of data in the discovery cohort, we determined the optimal threshold value, which was defined as the cutoff point with the smallest log-rank *P* value. The concordance index (c-index) or the Harrell *C* statistic was used to assess prognostic accuracy. The hazard ratio (HR) was used to measure the degree of survival differences for the stratified groups on the Kaplan-Meier plots. For the c-index and HRs, 95% confidence intervals (CIs) were also assessed. Data in patients alive at 10 years were censored at that time to alleviate confounding by comorbidities. The log-rank test and concordance index were used to assess prognostic performance. To adjust for multiple statistical testing, the Benjamini-Hochberg method (45) was used to control the false-discovery rate (FDR) in the univariate analysis. An FDR of less than 0.1 was considered to be statistically significant. The hypergeometric test was used to assess whether the genes of interest within a particular pathway were significantly overrepresented compared with those in random sampling. All statistical analyses were performed in R (R Foundation for Statistical Computing, Vienna, Austria).

Table 3

Univariate and Multivariate Analysis of Imaging Features Extracted from Tumor and Tumor-adjacent Parenchyma

	Univariate Analysis		Multivariate Analysis	
Location and Imaging Feature	Concordance Index	Wald *P* Value	Coefficient	Wald *P* Value
Tumor				
Volume*	0.70 (0.60, 0.80)	<.0001	….	…
FTV	0.73 (0.63, 0.82)	<.0001	0.40	.030
SER	0.53 (0.40, 0.65)	.69	0.07	.813
Parenchyma				
Correlation	0.64 (0.54, 0.74)	.006	1.14	.007
$Prop_{SER>1.5}$	0.62 (0.50, 0.72)	.037	−0.33	.370
$\overline{SER}_{1\%}$	0.56 (0.44, 0.67)	.34	−1.24	.004
Energy	0.54 (0.42, 0.66)	.56	−0.52	.613

Note.—Data in parentheses are 95% CIs.

* Volume was not included in the multivariate analysis because of its high correlation with FTV and lower univariate performance than FTV.

Results

Prognostic Evaluation of Tumor-adjacent Parenchymal Image Features

The prognostic accuracy of 10 parenchymal image features in association with RFS in the imaging discovery cohort is shown in Figure 2a. After adjustment for multiple hypothesis testing, only one image feature that measured heterogeneity of enhancement pattern achieved the predefined significance level (FDR < 0.1). A higher value of this correlation measure represents a higher degree of heterogeneity of enhancement. We further defined an optimal cutoff value of 0.57 for this image feature, which maximized the survival differences between subgroups in Kaplan-Meier analysis (Fig 2b) (log-rank *P* = .024, HR = 2.60, 95% CI: 1.43, 6.15). The Pearson correlation matrix of 10 image features is shown in Figure 2c. The output of the multivariate Cox model with four uncorrelated features is shown in Table E2 (online), where the information measure of correlation remained as having the strongest independent association with RFS (*P* = .009).

Parenchymal Features Provided Independent Prognostic Information to Tumor Features

There was little correlation between the three tumor image features and four uncorrelated parenchymal features (Pearson correlation < 0.50), as shown in Figure 2d. The multivariate analysis of uncorrelated image features from tumor and parenchyma

Figure 3

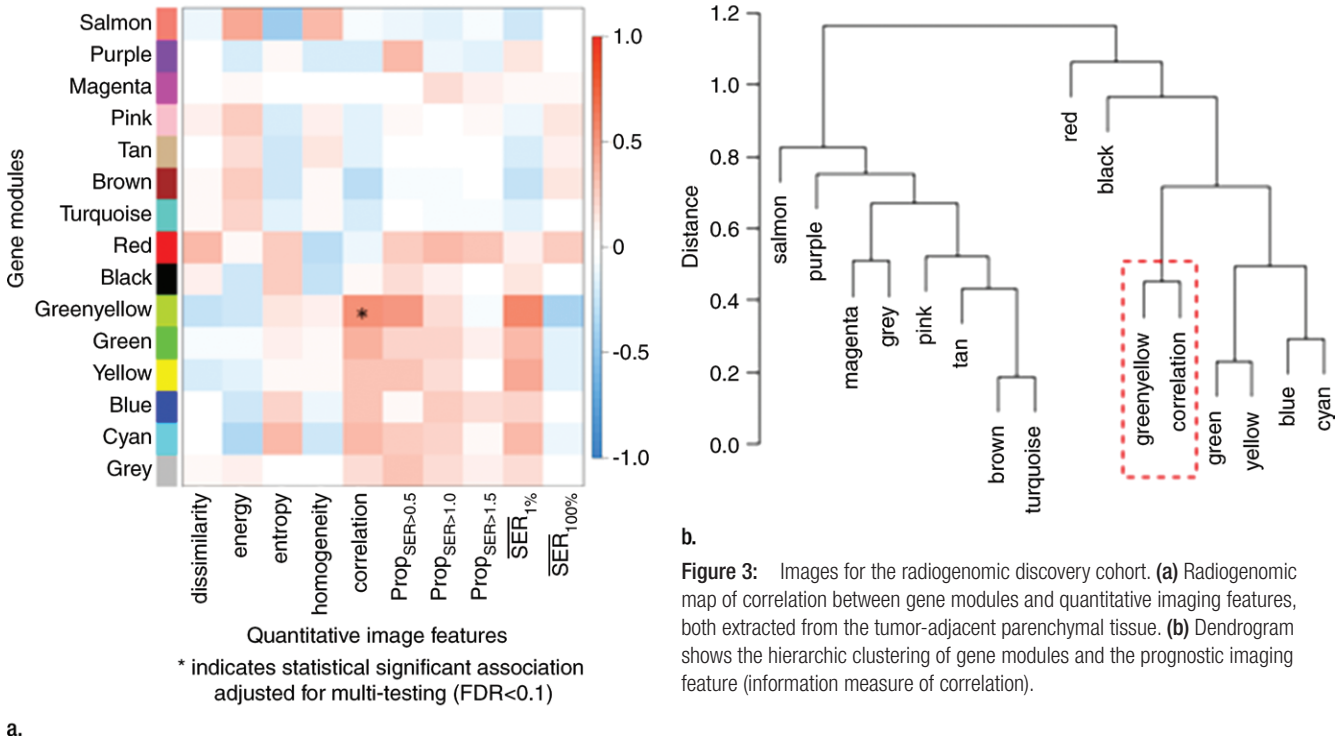

Figure 3: Images for the radiogenomic discovery cohort. **(a)** Radiogenomic map of correlation between gene modules and quantitative imaging features, both extracted from the tumor-adjacent parenchymal tissue. **(b)** Dendrogram shows the hierarchic clustering of gene modules and the prognostic imaging feature (information measure of correlation).

are reported in Table 3, where the information measure of correlation remained as independently associated with RFS (P = .007). Therefore, all subsequent radiogenomic analysis was focused on the information measure of correlation extracted from tumor-adjacent parenchyma.

Radiogenomic Map Linking Molecular and Imaging Phenotypes of Tumor-adjacent Parenchymal Tissue

On the basis of all available tumor-adjacent parenchymal samples (n = 114) in the TCGA cohort, we discovered 15 gene modules using WGCNA. We correlated each of these modules with each of the 10 parenchymal imaging features and created a radiogenomic map showing the pairwise association between gene modules and image features (Fig 3). After controlling for FDR, only one gene module (labeled as *greenyellow*) was significantly associated with the previously identified prognostic image feature, with a correlation coefficient of 0.55 (FDR = 0.08).

Molecular Correlates of the Tumor-adjacent Parenchymal Image Feature

The complete list of genes within the pinpointed *greenyellow* module is shown in Table 4. Using KEGG pathway enrichment analysis, we identified the tumor necrosis factor (TNF) signaling pathway as the most enriched pathway (hypergeometric $P < .0001$). Genes were mapped back to the TNF pathway and were related to six biologic processes, including leukocyte recruitment, inflammatory cytokines, intracellular signaling, cell adhesion, transcription factors, and synthesis of inflammatory mediators (Fig E1 [online]).

A 73-gene signature based on the tumor profiles in TCGA (n = 126) was built to assess associations with the tumor-adjacent parenchymal image feature (gray-level co-occurrence matrix information measure of correlation) and showed an R^2 of 0.873 and an adjusted R^2 of 0.38 (Fig E2 [online]). The complete gene signature is shown in Table 4 and Table E3 (online). For the 73 tumor genes in the signature, the TNF signaling pathway again appeared as the most enriched pathway (hypergeometric P = .007). Notably, the tumor genes were located upstream in the TNF signaling cascade, while genes from tumor-adjacent parenchyma were located downstream (Fig E1 [online]). Finally, on the basis of the predicted image feature using the 73-gene signature, we identified the significantly associated tumor genes (FDR < 0.1) in the independent TCGA testing cohort (subgroup 4, n = 879) and mapped them in the TNF signaling pathway (Fig E1 [online]). The number of tumor genes within this pathway remained overrepresented (hypergeometric P = .018).

Prognostic Relevance of the Tumor-adjacent Parenchymal Image Feature

As shown in Figure 4, for the independent TCGA testing cohort (subgroup 4), the predicted imaging feature using the 73-gene signature significantly stratified patients into two groups in

Table 4

Biologic Annotation for the 64 Genes from the Tumor-adjacent Parenchymal Gene Module (*Greenyellow*) and the 73 Genes in the Signature for the Parenchymal Image Feature

Process Category of Cancer Hallmarks	64 Genes in the Parenchymal Gene Module	73 Genes in the Signature
DNA damage	*CSF3, SELE, IL6, FOSB, NR4A1, SERPINE1, ATF3, FOS, JUNB, CYR61, DUSP1, BTG2*	*UROD*
Immune	*IL6, SOCS3, PTGS2, IL1B, SERPINE1, CCL2, IL8, OSM, LIF, CCL4, RGS16, IL13, CD69, CDKN1A, PIM1, HBEGF, MAFF, BTG2, GPR183*	*IFI30*
Metabolic	*SERPINE1, CH25H, STC1, BTG2*	*DDIT4, TIMM8B, NDUFB1, UROD, SLC25A3, ECHS1, ERP29, PGAM1, ALDH2, GNE, GSTZ1*
Pathway	*IL6, EGR3, IL1B, SERPINE1, ATF3, CCL2, ZFP36, JUNB, CYR61, CD69, GADD45B, STC1, CDKN1A, PIM1, DUSP1, MAFF, CTGF, BTG2*	*DDIT4*
Proliferation	*ATF3, FOS, LIF, KLF4, SLC2A3, RGS16, CDKN1A, HBEGF, PLK3, BTG2*	*DDIT4, SLC25A3, PSIP1, IFI30, GM2A*
Signaling	*IL6, NR4A3, FOSB, NR4A1, SOCS3, PTGS2, FOSL1, EGR3, IL1B, SERPINE1, ATF3, CCL2, FOS, EGR2, ZFP36, LIF, EGR1, CCL4, JUNB, KLF4, SLC2A3, NR4A2, RGS16, CYR61, IL13, CD69, GADD45B, STC1, CDKN1A, KLF2, PIM1, HBEGF, DUSP1, SIK1, IER2, ADAMTS1, MAFF, BTG2, GPR183*	*DDIT4, MTHFR, MAP2 K6, IFI30*
Development	*IL6, SERPINE1, IL8, CYR61, GADD45B, STC1, CDKN1A, HBEGF, CTGF*	*ECHS1, SGCB, ALDH2*
Others	*C2CD4B, CCL3 L1, ADAMTS4, CCL4 L2, LOC100302650, AG2, CCL3, RND1, ODF3 L1, SLC2A14, CSRNP1, EGR4, FILIP1 L, RNF122, SLC25A25, DUSP10, C8orf77, SNORA39*	*GAS2 L2*, LOC285501*, LOC728758*, AGTRAP, SLC24A6, KIAA2026, SEPT12, C11orf59, TOM1 L2, VTI1B, AWAT2*, GCHFR, HMGN4, OTUB2, SNAPC3, ZDHHC13, GPR150, KLHL23, TRMT11, PIN4, ITCH, WBSCR16, KIAA1908*, CCDC91, ZNF34, HIST1H2AM, LOC100134868*, IDI2*, HIST1H2BG, LOC650368*, MATK, SIL1, RNF181, DCAF12, C14orf169, HIST1H3D, ZNF146, LOC285419*, ZNF192, TAF3, HACE1, UPF2, FAM102B, COMMD1, HIST2H3D, PHF23, ZNF585B, DNAJC24, ROMO1, FAM109A, LOC127841*, GNPDA2, HYI, ZNF567, C12orf45, ZNF527*

Note.—The process category of cancer hallmarks was used as previously defined (49).

* Indicate one of 10 nonoverlapped genes from the 73-gene signature during validation in the GSE 1456.

terms of RFS (log-rank P = .029; HR = 1.54 [95% CI: 1.03, 2.29]) and overall survival (log-rank P = .042; HR = 1.51 [95% CI: 1.02, 2.28]). In another independent cohort (GSE 1456), the patients were divided into two subgroups according to hierarchic clustering based on the expression of 63 overlapped genes (see gene list in Table 4), as shown in Figure 5, and this stratification was significant (log-rank P = .00058, HR = 2.84, and 95% CI: 1.53, 5.29 for RFS and log-rank P = .0026, HR = 2.92, and 95% CI: 1.40, 6.08 for overall survival).

Discussion

The enhancement pattern of breast parenchyma at dynamic contrast-enhanced MR imaging has recently been shown to be a promising imaging marker for the risk of developing breast cancer. Since the initial report on its potential diagnostic value (50), breast parenchymal enhancement has been integrated into routine clinical breast MR imaging reports according to the Breast Imaging Reporting and Data System (51). In addition to this potential role in diagnosis, imaging characteristics of parenchyma have been associated with breast cancer outcomes such as treatment response, local recurrence, and survival (17,18,22,23,25,26,52), but their biologic underpinning is poorly understood. We aimed to elucidate the molecular basis of quantitative imaging characteristics of tumor-adjacent parenchyma by integrating spatially congruent imaging and gene expression data. Furthermore, we constructed a 73-gene signature of the parenchymal imaging feature and confirmed its prognostic value for RFS and overall survival in two large independent breast cancer

Figure 4

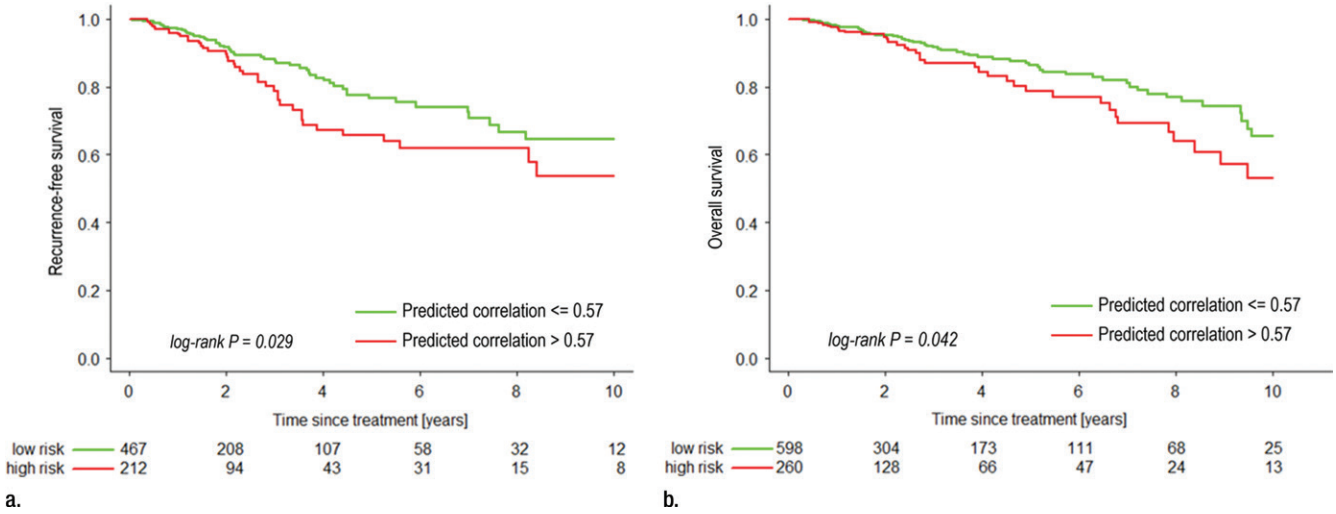

Figure 4: Kaplan-Meier curves of (**a**) RFS and (**b**) overall survival for the independent TCGA testing cohort (subgroup 4).

cohorts that included more than 1000 patients.

Prognostic biomarkers are critically needed to optimize breast cancer care. Various studies have evaluated gene expression signatures to predict breast cancer prognosis (53,54). This molecular approach is limited by its cost, requirement for invasive surgery or biopsy, and potential for sampling bias caused by the intratumor heterogeneity of breast cancer (55,56). Moreover, there is no clinically prognostic gene signature test for estrogen receptor–negative tumors, which account for about one-third of all breast cancers (57). By contrast, imaging represents a unique opportunity for noninvasive interrogation of the entire tumor as well as its surrounding tissues, and it can potentially provide useful complementary information to molecular analysis.

Our radiogenomic study differs from previous radiogenomic work in two aspects. First, previous studies have focused on finding imaging correlates of molecular features (36,58–67) such as the OncotypeDx 21-gene recurrence score. We reversed the study design, aiming to reveal the molecular pathways associated with specific imaging markers. One recent study used this approach to show that epithelial-mesenchymal transition is associated with maximum standardized uptake value at fluorine 18 fluorodeoxyglucose positron emission tomography in non–small cell lung cancer (68). A second distinction is that prior radiogenomic studies have focused image analysis on the tumor, while we specifically analyzed the tumor-adjacent parenchymal tissue.

This study discovered that the TNF signaling pathway is associated with the tumor-adjacent parenchymal image feature that is associated with poor breast cancer prognosis. TNF promotes inflammation and invasive growth of tumor cells (69,70). Along with activated macrophages, the major source of TNF production, tumor cells, including B-cell lymphoma and breast cancers, can also express TNF (69). TNF has been implicated in many oncogenic processes, including epithelial-mesenchymal transition (71,72), proliferation (73), angiogenesis (74), invasion, and metastasis (75–77).

Limitations of this study included its retrospective nature and the small size of the radiogenomic discovery cohort. While including the large, multi-institution TCGA cohort enhanced statistical power and external validity, it also introduced uncertainty because of the diversity of imaging acquisition protocols in TCGA. Another limitation is the relatively short follow-up time for TCGA cohort compared with the other two cohorts, which might influence the outcome data. Our identification of molecular processes that were significantly associated with parenchymal imaging features is hypothesis generating. Further mechanistic evidence is essential to confirm these results and pinpoint molecular switches that drive the imaging phenotype reported here.

We focused on molecular analysis at the transcriptome level. In future, incorporating other types of "-omics" data, such as genetic mutation and copy number variation, could provide a more complete picture of the molecular characteristics (59). Although we demonstrated associations with prognosis in two large independent cohorts using a gene expression signature of the imaging feature, future study should directly validate results using large cohorts of patients with both imaging and survival data available.

In conclusion, we demonstrate an association between the imaging and molecular phenotypes of tumor-adjacent parenchyma and clinical outcomes in breast cancer. These results shed important light on the underlying biology behind prognostic imaging markers, which may ultimately inform prevention and treatment strategies.

Acknowledgment: The authors thank The Cancer Imaging Archive for providing the breast cancer cases enrolled in TCGA study.

Figure 5

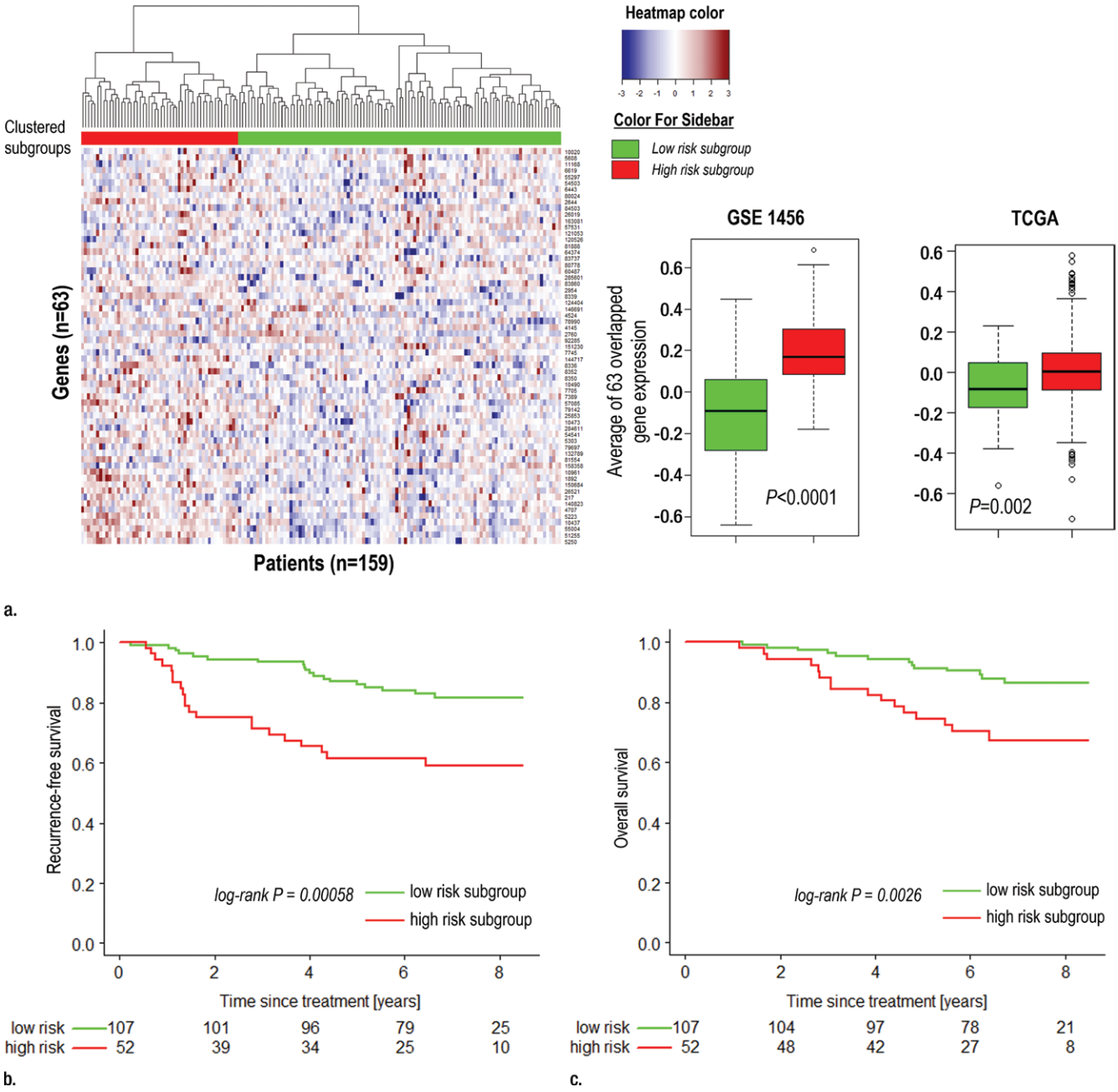

Figure 5: Images for the GSE 1456 cohort. **(a)** The details of patient stratification based on hierarchic clustering of the 63 measured tumor genes in the 73-gene signature, as well as **(b, c)** Kaplan-Meier curves of RFS (**b**) and overall survival (**c**).

Disclosures of Conflicts of Interest: J.W. disclosed no relevant relationships. **B.L.** disclosed no relevant relationships. **X.S.** disclosed no relevant relationships. **G.C.** disclosed no relevant relationships. **D.L.R.** disclosed no relevant relationships. **S.N.** Activities related to the present article: disclosed no relevant relationships. Activities not related to the present article: is on the scientific advisory boards of Fovia, EchoPixel, and Radlogics; holds stock or stock options in EchoPixel; is a consultant for Carestream. Other relationships: disclosed no relevant relationships. **D.M.I.** disclosed no relevant relationships. **A.W.K.** disclosed no relevant relationships. **R.L.** disclosed no relevant relationships.

References

1. Siegel RL, Miller KD, Jemal A. Cancer statistics, 2016. CA Cancer J Clin 2016;66(1):7–30.

2. Abrams JS. Adjuvant therapy for breast cancer--results from the USA consensus conference. Breast Cancer 2001;8(4):298–304.

3. Early Breast Cancer Trialists' Collaborative Group (EBCTCG), Davies C, Godwin J, et al. Relevance of breast cancer hormone receptors and other factors to the efficacy of adjuvant tamoxifen: patient-level meta-analysis of randomised trials. Lancet 2011;378(9793):771–784.
4. Sparano JA, Gray RJ, Makower DF, et al. Prospective validation of a 21-gene expression assay in breast cancer. N Engl J Med 2015;373(21):2005–2014.
5. Bhooshan N, Giger ML, Jansen SA, Li H, Lan L, Newstead GM. Cancerous breast lesions on dynamic contrast-enhanced MR images: computerized characterization for image-based prognostic markers. Radiology 2010;254(3):680–690.
6. Mahoney MC, Gatsonis C, Hanna L, DeMartini WB, Lehman C. Positive predictive value of BI-RADS MR imaging. Radiology 2012;264(1):51–58.
7. Li X, Abramson RG, Arlinghaus LR, et al. Multiparametric magnetic resonance imaging for predicting pathological response after the first cycle of neoadjuvant chemotherapy in breast cancer. Invest Radiol 2015;50(4):195–204.
8. Hylton NM, Blume JD, Bernreuter WK, et al. Locally advanced breast cancer: MR imaging for prediction of response to neoadjuvant chemotherapy—results from ACRIN 6657/I-SPY TRIAL. Radiology 2012;263(3):663–672.
9. Berg WA, Gutierrez L, NessAiver MS, et al. Diagnostic accuracy of mammography, clinical examination, US, and MR imaging in preoperative assessment of breast cancer. Radiology 2004;233(3):830–849.
10. Sutton EJ, Dashevsky BZ, Oh JH, et al. Breast cancer molecular subtype classifier that incorporates MRI features. J Magn Reson Imaging 2016;44(1):122–129.
11. Pickles MD, Lowry M, Gibbs P. Pretreatment prognostic value of dynamic contrast-enhanced magnetic resonance imaging vascular, texture, shape, and size parameters compared with traditional survival indicators obtained from locally advanced breast cancer patients. Invest Radiol 2016;51(3):177–185.
12. Waugh SA, Purdie CA, Jordan LB, et al. Magnetic resonance imaging texture analysis classification of primary breast cancer. Eur Radiol 2016;26(2):322–330.
13. Burnside ES, Drukker K, Li H, et al. Using computer-extracted image phenotypes from tumors on breast magnetic resonance imaging to predict breast cancer pathologic stage. Cancer 2016;122(5):748–757.
14. Parikh J, Selmi M, Charles-Edwards G, et al. Changes in primary breast cancer heterogeneity may augment midtreatment MR imaging assessment of response to neoadjuvant chemotherapy. Radiology 2014;272(1):100–112.
15. Yi A, Cho N, Im SA, et al. Survival outcomes of breast cancer patients who receive neoadjuvant chemotherapy: association with dynamic contrast-enhanced MR imaging with computer-aided evaluation. Radiology 2013;268(3):662–672.
16. Hylton NM, Gatsonis CA, Rosen MA, et al. Neoadjuvant chemotherapy for breast cancer: functional tumor volume by MR imaging predicts recurrence-free survival-results from the ACRIN 6657/CALGB 150007 I-SPY 1 TRIAL. Radiology 2016;279(1):44–55.
17. King V, Brooks JD, Bernstein JL, Reiner AS, Pike MC, Morris EA. Background parenchymal enhancement at breast MR imaging and breast cancer risk. Radiology 2011;260(1):50–60.
18. Dontchos BN, Rahbar H, Partridge SC, et al. Are qualitative assessments of background parenchymal enhancement, amount of fibroglandular tissue on MR images, and mammographic density associated with breast cancer risk? Radiology 2015;276(2):371–380.
19. Telegrafo M, Rella L, Stabile Ianora AA, Angelelli G, Moschetta M. Breast MRI background parenchymal enhancement (BPE) correlates with the risk of breast cancer. Magn Reson Imaging 2016;34(2):173–176.
20. Bennani-Baiti B, Baltzer PA. Reply to "Breast MRI background parenchymal enhancement (BPE) correlates with the risk of breast cancer". Magn Reson Imaging 2016;34(9):1337–1338.
21. Bennani-Baiti B, Dietzel M, Baltzer PA. MRI background parenchymal enhancement is not associated with breast cancer. PLoS One 2016;11(7):e0158573.
22. Preibsch H, Wanner L, Bahrs SD, et al. Background parenchymal enhancement in breast MRI before and after neoadjuvant chemotherapy: correlation with tumour response. Eur Radiol 2016;26(6):1590–1596.
23. van der Velden BH, Dmitriev I, Loo CE, Pijnappel RM, Gilhuijs KG. Association between parenchymal enhancement of the contralateral breast in dynamic contrast-enhanced MR imaging and outcome of patients with unilateral invasive breast cancer. Radiology 2015;276(3):675–685.
24. Hu M, Yao J, Carroll DK, et al. Regulation of in situ to invasive breast carcinoma transition. Cancer Cell 2008;13(5):394–406.
25. Hattangadi J, Park C, Rembert J, et al. Breast stromal enhancement on MRI is associated with response to neoadjuvant chemotherapy. AJR Am J Roentgenol 2008;190(6):1630–1636.
26. Kim SA, Cho N, Ryu EB, et al. Background parenchymal signal enhancement ratio at preoperative MR imaging: association with subsequent local recurrence in patients with ductal carcinoma in situ after breast conservation surgery. Radiology 2014;270(3):699–707.
27. The Cancer Imaging Archive (TCIA). http://www.cancerimagingarchive.net. Accessed October 31, 2016.
28. Li KL, Partridge SC, Joe BN, et al. Invasive breast cancer: predicting disease recurrence by using high-spatial-resolution signal enhancement ratio imaging. Radiology 2008;248(1):79–87.
29. Jafri NF, Newitt DC, Kornak J, Esserman LJ, Joe BN, Hylton NM. Optimized breast MRI functional tumor volume as a biomarker of recurrence-free survival following neoadjuvant chemotherapy. J Magn Reson Imaging 2014;40(2):476–482.
30. Cancer Genome Atlas Network. Comprehensive molecular portraits of human breast tumours. Nature 2012;490(7418):61–70.
31. Casbas-Hernandez P, Sun X, Roman-Perez E, et al. Tumor intrinsic subtype is reflected in cancer-adjacent tissue. Cancer Epidemiol Biomarkers Prev 2015;24(2):406–414.
32. Genomic Data Commons Data Portal. https://gdc-portal.nci.nih.gov/. Accessed October 31, 2016.
33. Pawitan Y, Bjöhle J, Amler L, et al. Gene expression profiling spares early breast cancer patients from adjuvant therapy: derived and validated in two population-based cohorts. Breast Cancer Res 2005;7(6):R953–R964.
34. Nabavizadeh N, Klifa C, Newitt D, et al. Topographic enhancement mapping of the cancer-associated breast stroma using breast MRI. Integr Biol 2011;3(4):490–496.
35. Dougherty ER, Lotufo RA. Hands-on morphological image processing (SPIE Tutorial Texts in Optical Engineering Vol TT59). Bellingham, Wash: International Society for Optical Engineering, 2003.
36. Wang J, Kato F, Oyama-Manabe N, et al. Identifying triple-negative breast cancer using background parenchymal enhancement heterogeneity on dynamic contrast-enhanced MRI: a pilot radiomics study. PLoS One 2015;10(11):e0143308.
37. Haralick RM, Shanmugam K, Dinstein I. Textural features for image classification. IEEE Trans Cybern 1973;SMC-3(6):610–621.
38. Tustison NJ, Avants BB, Cook PA, et al. N4ITK: improved N3 bias correction. IEEE Trans Med Imaging 2010;29(6):1310–1320.
39. Barajas RF Jr, Hodgson JG, Chang JS, et al. Glioblastoma multiforme regional genetic and cellular expression patterns: influence on anatomic and physiologic MR imaging. Radiology 2010;254(2):564–576.

40. Partridge SC, Gibbs JE, Lu Y, et al. MRI measurements of breast tumor volume predict response to neoadjuvant chemotherapy and recurrence-free survival. AJR Am J Roentgenol 2005;184(6):1774–1781.
41. Pickles MD, Manton DJ, Lowry M, Turnbull LW. Prognostic value of pre-treatment DCE-MRI parameters in predicting disease free and overall survival for breast cancer patients undergoing neoadjuvant chemotherapy. Eur J Radiol 2009;71(3):498–505.
42. Johansen R, Jensen LR, Rydland J, et al. Predicting survival and early clinical response to primary chemotherapy for patients with locally advanced breast cancer using DCE-MRI. J Magn Reson Imaging 2009;29(6):1300–1307.
43. Pickles MD, Lowry M, Manton DJ, Turnbull LW. Prognostic value of DCE-MRI in breast cancer patients undergoing neoadjuvant chemotherapy: a comparison with traditional survival indicators. Eur Radiol 2015;25 (4):1097–1106.
44. Langfelder P, Horvath S. WGCNA: an R package for weighted correlation network analysis. BMC Bioinformatics 2008;9(1):559.
45. Benjamini Y, Hochberg Y. Controlling the false discovery rate: a practical and powerful approach to multiple testing. J R Stat Soc Series B Stat Methodol 1995;57(1):289–300.
46. KEGG: Kyoto Encyclopedia of Genes and Genomes. http://www.genome.jp/kegg/. Accessed September 30, 2016.
47. Murtagh F, Legendre P. Ward's hierarchical agglomerative clustering method: which algorithms implement ward's criterion? J Classif 2014;31(3):274–295.
48. Tibshirani R, Walther G, Hastie T. Estimating the number of clusters in a data set via the gap statistic. J R Stat Soc Series B Stat Methodol 2001;63(2):411–423.
49. Liberzon A, Birger C, Thorvaldsdóttir H, Ghandi M, Mesirov JP, Tamayo P. The Molecular Signatures Database (MSigDB) hallmark gene set collection. Cell Syst 2015;1(6):417–425.
50. Van Goethem M, Schelfout K, Kersschot E, et al. Enhancing area surrounding breast carcinoma on MR mammography: comparison with pathological examination. Eur Radiol 2004;14(8):1363–1370.
51. Edwards SD, Lipson JA, Ikeda DM, Lee JM. Updates and revisions to the BI-RADS magnetic resonance imaging lexicon. Magn Reson Imaging Clin N Am 2013;21(3):483–493.
52. Wu J, Cui Y, Sun X, et al. Unsupervised clustering of quantitative image phenotypes reveals breast cancer subtypes with distinct prognoses and molecular pathways. Clin Cancer Res 2017 Jan 10. [Epub ahead of print]
53. van de Vijver MJ, He YD, van't Veer LJ, et al. A gene-expression signature as a predictor of survival in breast cancer. N Engl J Med 2002;347(25):1999–2009.
54. Gingras I, Desmedt C, Ignatiadis M, Sotiriou C. CCR 20th Anniversary Commentary: Gene-expression signature in breast cancer--where did it start and where are we now? Clin Cancer Res 2015;21(21):4743–4746.
55. Barry WT, Kernagis DN, Dressman HK, et al. Intratumor heterogeneity and precision of microarray-based predictors of breast cancer biology and clinical outcome. J Clin Oncol 2010;28(13):2198–2206.
56. Martelotto LG, Ng CK, Piscuoglio S, Weigelt B, Reis-Filho JS. Breast cancer intratumor heterogeneity. Breast Cancer Res 2014;16(3):210.
57. Győrffy B, Hatzis C, Sanft T, Hofstatter E, Aktas B, Pusztai L. Multigene prognostic tests in breast cancer: past, present, future. Breast Cancer Res 2015;17(1):11.
58. Yamamoto S, Han W, Kim Y, et al. Breast cancer: radiogenomic biomarker reveals associations among dynamic contrast-enhanced MR imaging, long noncoding RNA, and metastasis. Radiology 2015;275(2):384–392.
59. Zhu Y, Li H, Guo W, et al. Deciphering genomic underpinnings of quantitative MRI-based radiomic phenotypes of invasive breast carcinoma. Sci Rep 2015;5:17787.
60. Ashraf AB, Daye D, Gavenonis S, et al. Identification of intrinsic imaging phenotypes for breast cancer tumors: preliminary associations with gene expression profiles. Radiology 2014;272(2):374–384.
61. Sutton EJ, Oh JH, Dashevsky BZ, et al. Breast cancer subtype intertumor heterogeneity: MRI-based features predict results of a genomic assay. J Magn Reson Imaging 2015;42(5):1398–1406.
62. Yamamoto S, Maki DD, Korn RL, Kuo MD. Radiogenomic analysis of breast cancer using MRI: a preliminary study to define the landscape. AJR Am J Roentgenol 2012;199(3):654–663.
63. Li H, Zhu Y, Burnside ES, et al. MR imaging radiomics signatures for predicting the risk of breast cancer recurrence as given by research versions of MammaPrint, Oncotype DX, and PAM50 gene assays. Radiology 2016;281(2):382–391.
64. Agner SC, Rosen MA, Englander S, et al. Computerized image analysis for identifying triple-negative breast cancers and differentiating them from other molecular subtypes of breast cancer on dynamic contrast-enhanced MR images: a feasibility study. Radiology 2014;272(1):91–99.
65. Mazurowski MA, Zhang J, Grimm LJ, Yoon SC, Silber JI. Radiogenomic analysis of breast cancer: luminal B molecular subtype is associated with enhancement dynamics at MR imaging. Radiology 2014;273(2):365–372.
66. Guo W, Li H, Zhu Y, et al. Prediction of clinical phenotypes in invasive breast carcinomas from the integration of radiomics and genomics data. J Med Imaging (Bellingham) 2015;2(4):041007.
67. Wu J, Sun X, Wang J, et al. Identifying relations between imaging phenotypes and molecular subtypes of breast cancer: Model discovery and external validation. J Magn Reson Imaging 2017 Feb 8. [Epub ahead of print]
68. Yamamoto S, Huang D, Du L, et al. Radiogenomic analysis demonstrates associations between (18)F-fluoro-2-deoxyglucose PET, prognosis, and epithelial-mesenchymal transition in non-small cell lung cancer. Radiology 2016;280(1):261–270.
69. Bigatto V, De Bacco F, Casanova E, et al. TNF-α promotes invasive growth through the MET signaling pathway. Mol Oncol 2015;9(2):377–388.
70. Wu Y, Zhou BP. TNF-alpha/NF-kappaB/Snail pathway in cancer cell migration and invasion. Br J Cancer 2010;102(4):639–644.
71. Bates RC, Mercurio AM. Tumor necrosis factor-α stimulates the epithelial-to-mesenchymal transition of human colonic organoids. Mol Biol Cell 2003;14(5):1790–1800.
72. Thiery JP, Acloque H, Huang RY, Nieto MA. Epithelial-mesenchymal transitions in development and disease. Cell 2009;139(5):871–890.
73. Montesano R, Soulié P, Eble JA, Carrozzino F. Tumour necrosis factor α confers an invasive, transformed phenotype on mammary epithelial cells. J Cell Sci 2005;118(Pt 15):3487–3500.
74. Leibovich SJ, Polverini PJ, Shepard HM, Wiseman DM, Shively V, Nuseir N. Macrophage-induced angiogenesis is mediated by tumour necrosis factor-α. Nature 1987;329 (6140):630–632.
75. Balkwill F. TNF-α in promotion and progression of cancer. Cancer Metastasis Rev 2006;25(3):409–416.
76. Malik ST, Naylor MS, East N, Oliff A, Balkwill FR. Cells secreting tumour necrosis factor show enhanced metastasis in nude mice. Eur J Cancer 1990;26(10):1031–1034.
77. Orosz P, Echtenacher B, Falk W, Rüschoff J, Weber D, Männel DN. Enhancement of experimental metastasis by tumor necrosis factor. J Exp Med 1993;177(5):1391–1398.